Sheffield Hallam University

Tabletop Testbed for Attitude Determination and Control of Nanosatellites

SILVA, R.C.D., GUIMARÃES, F.C., LOIOLA, J.V.L.D., BORGES, R.A., BATTISTINI, Simone <http://orcid.org/0000-0002-0491-0226> and CAPPELLETTI, C.

Citation:

Tabletop testbed for attitude determination and control of nanosatellites

Rodrigo Cardoso da Silva[1], Fernando Cardoso Guimarães[2], João Victor Lopes de Loiola[3], Renato Alves Borges[4], Simone Battistini[5], and Chantal Cappelletti[6]

[1]Postgraduate student, Department of Electrical Engineering, University of Brasília, Campus Darcy Ribeiro, Brasília-DF, CEP 70910-900, Brazil (e-mail: rcsilva@lara.unb.br)

[2]Postgraduate student, Department of Electrical Engineering, University of Brasília, Campus Darcy Ribeiro, Brasília-DF, CEP 70910-900, Brazil (e-mail: fguimaraes@lara.unb.br)

[3]Postgraduate student, Department of Electrical Engineering, University of Brasília, Campus Darcy Ribeiro, Brasília-DF, CEP 70910-900, Brazil (e-mail: victor@lara.unb.br)

[4]Ph.D., Assistant professor, Department of Electrical Engineering, University of Brasília, Campus Darcy Ribeiro, Brasília-DF, CEP 70910-900, Brazil (e-mail: raborges@ene.unb.br)

[5]Ph.D., Assistant professor, Faculty of Gama, University of Brasília, Campus Gama, Gama-DF, CEP 72444-240, Brazil (e-mail: simone.battistini@aerospace.unb.br)

[6]Ph.D., Assistant professor, Department of Mechanical, Materials and Manufacturing Engineering, University of Nottingham, Nottingham NG7 2RD, United Kingdom (e-mail: chantal.cappelletti@nottingham.ac.uk)

ABSTRACT

In order to simulate the conditions of the space environment at ground, the Laboratory of Application and Innovation in Aerospace Science (LAICA) of the University of Brasília (UnB) is developing a dedicated testbed aiming at reproducing nanosatellite attitude motion. The testbed is composed of an air bearing table and a Helmholtz cage. The air bearing table is a spacecraft simulator that can simulate frictionless conditions with three rotational degrees of freedom. Balancing the simulator is essential in order to make the gravitational torque negligible. The testbed

is also equipped with a Helmholtz cage whose purpose is to recreate the Earth magnetic field conditions that spacecrafts encounter in orbit. The design and realization of this low-cost testbed is presented in this paper. A simple and efficient automated balancing algorithm based on the Least Squares Method (LSM) is proposed and validated by experiments. The performance of the proposed simulator is evaluated and compared with previous works.

INTRODUCTION

In view of the great complexity and high budgets which usually concern spacecraft projects, it is highly desirable to perform tests on ground-based platforms to reduce the implicated risks. The effectiveness of taking tests on those platforms is closely related to their capacity to simulate the peculiarities of the space environment. For instance, the absence of atmosphere, the presence of microgravity and the magnetic field of Earth are characteristics that directly affect the design of spacecrafts attitude determination and control systems.

Since the beginning of the space race, air bearing based platforms have been used as testbeds for simulating spacecraft attitude motion. Depending on the number of degrees of freedom (DOF) provided, these platforms can be classified as planar, rotational or combinational. Planar systems provide two translational degrees of freedom and, occasionally, a rotational degree of freedom (Schwartz et al. 2003).

The focus in this work is on the rotational systems, which aim to provide a frictionless rotational movement with three degrees of freedom. The inherent difficulty of this type of platform is to achieve this rotational freedom, leading the platform to some common build standards, such as those named tabletop, umbrella and dumbell (Schwartz et al. 2003). Since the tabletop design is used in this work, special attention is given to this configuration, which is depicted in Fig. 1. In this type of platform, the table is mounted directly on the air bearing. Although the rotational movement is constrained by the mounting plate and the hemisphere design, this is the most common design between the rotational systems as it is easier to balance when compared with umbrella and dumbell systems. Examples of tabletop designs are shown in Kim and Agrawal (2006) and Saulnier et al. (2013).
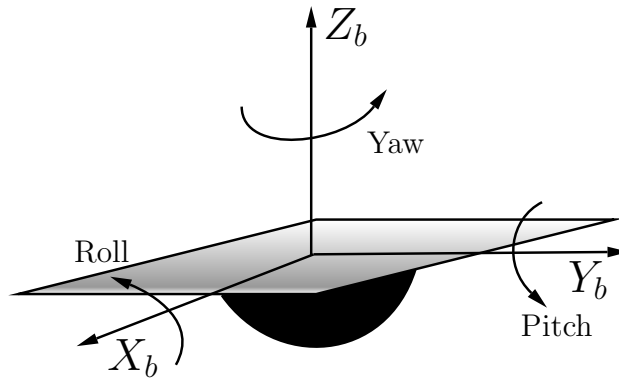
Fig. 1. Attitude angles in tabletop configuration.

Combinational systems are those which combine the features of both planar and rotational systems. For this reason, these platforms often provide 5 to 6 degrees of freedom. An example of combinational system is given in Gallardo and Bevilacqua (2011), which is a dynamic 6 DOF simulator. This platform is composed of two stages, one responsible for rotational motion and the other responsible for translational motion in a approximately $18m^2$ epoxy floor.

Common to all of these types of platform is the need of an efficient balancing procedure. The purpose of this balancing is to reduce the gravitational torque experienced by the platform. In order to accomplish this, the center of mass (CM) of the platform must be placed as close as possible to its center of rotation (CR), *i.e.* the unbalance vector magnitude must be as close as possible to zero. In Mittelsteadt and Mehiel (2007), it is reported the importance of distributing the masses as symmetrically as possible and it is reserved space in the initial project for implementation of an automatic mass balancing system. This problem is often solved manually, as shown in Romano and Agrawal (2003) and Peck et al. (2003), in which a minimum gravitational torque of $0.01\ N \cdot m$, approximately, was achieved. In Carrara and Milani (2007), the need of balancing the system is mentioned, as well as the adopted procedure for accomplishing it manually. There are also numerical algorithms that search for the optimal placement for each equipment to be embedded in the platform (Xu et al. 2016). Another recent work addresses the necessity of implementing a balancing procedure (Carletta and Teofilatto 2017). In Thomas et al. (2018), the intent of implementing a CubeSat simulator, similar to the one described in this work, is presented. Moreover, the same

Silva, Approved on June 18th, 2018

balancing method described in this work is set as the start point for solving the balancing problem in Thomas et al. (2018), showing that this approach is being addressed nowadays in other facilities over the world.

Manual balancing procedures may take hours to get appropriate results. For this reason, other algorithms are based on automated processes, such as the algorithm presented in Kim and Agrawal (2009), which is an adaptive control scheme developed using Lyapunov theory. Other studies on adaptive control use, additionally, the Unscented Kalman Filter for tuning the vertical component of the unbalance vector (Chesi et al. 2013).

In this work, aiming to provide a cost-effective solution for the balancing problem, the simple and efficient well-known Least Squares Method (LSM) will be adapted and used to provide batch estimations of the unbalance vector of the platform (Silva et al. 2016).

This paper presents an Attitude Determination and Control Systems (ADCS) testbed composed of an air bearing table and a Helmholtz cage, being developed at the LAICA. This platform aims at simulating two key conditions present in the in-orbit environment: the magnetic field of the Earth and the frictionless conditions of rotations in space.

The air bearing table is installed inside the Helmholtz cage, a device used to induce a magnetic field around the structure of the cage. In particular, inside the cage the induced magnetic field can be adjusted in order to recreate the Earth magnetic field conditions that spacecrafts encounters in orbit.

This paper is an extension of the work presented in Silva et al. (2016). More experiments were run and further details were studied. This article is divided as follows. The second section shows a description of the air bearing platform developed for testing nanosatellites, including an overview of its physical parts and the hardware/software architecture. A description of the assembly aspects involved with the project of the Helmholtz cage is also presented. The third section provides an explanation of the balancing algorithm used and its theoretical foundations. The fourth section shows some tests made to evaluate the performance of the algorithm used to make the air bearing table balancing. Also, a comparative analysis with other balancing methods found in the literature

is made. Conclusions are given in the fifth section.

SYSTEM CONFIGURATION

This section describes the components of the proposed testbed in two separated subsections. The first subsection addresses the constructive aspects of the hardware and the organization of the software of the air bearing table. The second subsection presents the Helmholtz cage principle with a description of its structure. The capability of magnetic field generation of the Helmholtz cage is illustrated with a set of measurements.

The air bearing table

The air bearing table was conceived for testing attitude determination and control algorithms for nanosatellites. The air bearing table developed at LAICA is an air bearing platform in the tabletop configuration, as it is shown in Fig. 2 (Schwartz et al. 2003). In other words, the table is mounted directly on the semisphere of the air bearing set. One major disadvantage of this configuration is the limitation in the excursion of the roll and pitch angles, which will not exceed $\pm 45°$. Nevertheless, this excursion is sufficient for all the tests that will be carried and, as will be seen in the section "BALANCING TECHNIQUES", full range is not required for the balancing algorithm to provide a consistent estimation of the unbalance vector.

The Movable Mass Units (MMU), Fig. 3, are responsible for adjusting the position of the center of mass and have two degrees of freedom, even though only one is used in each of the three MMUs. The two degrees of freedom of this device are accessible via a crank. In order to make this movement automatic and controllable by the electronic system, a motor is mounted in place of this crank for each MMU.

The electronic system that is embedded in the table contains:

1. Microcontroller: a complete USB-based microcontroller development system implemented on the ATMEGA8 microcontroller is used. This platform, which is compatible with Arduino software and libraries, controls all the electronic components embedded in the balancing system of the air bearing table.
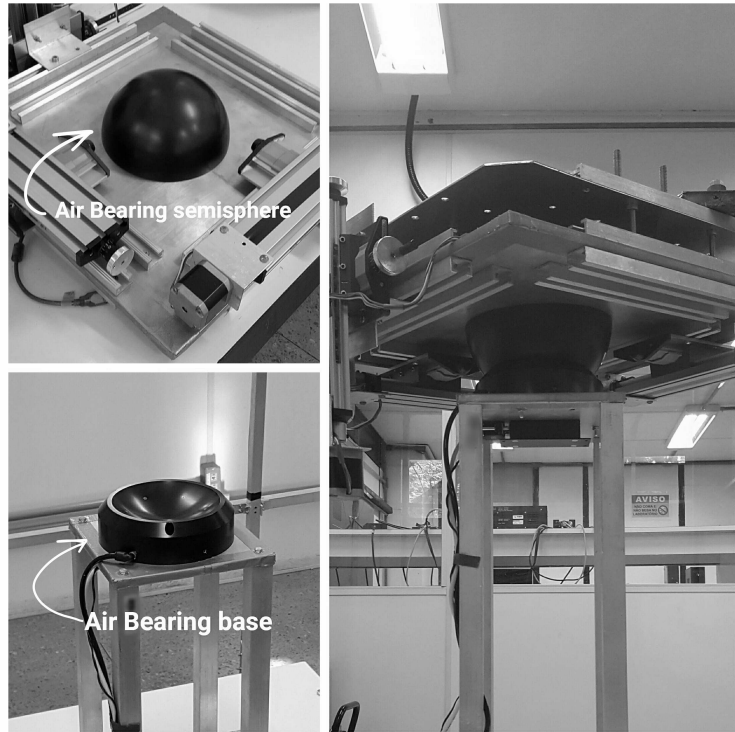
Fig. 2. The air bearing assembly.
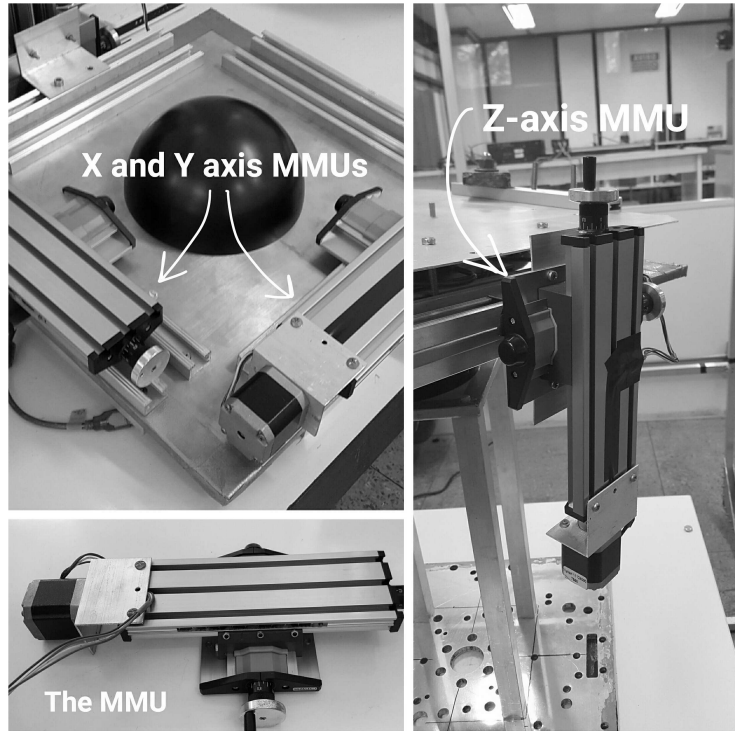
Fig. 3. The Movable Mass Units (MMUs).

Silva, Approved on June 18th, 2018
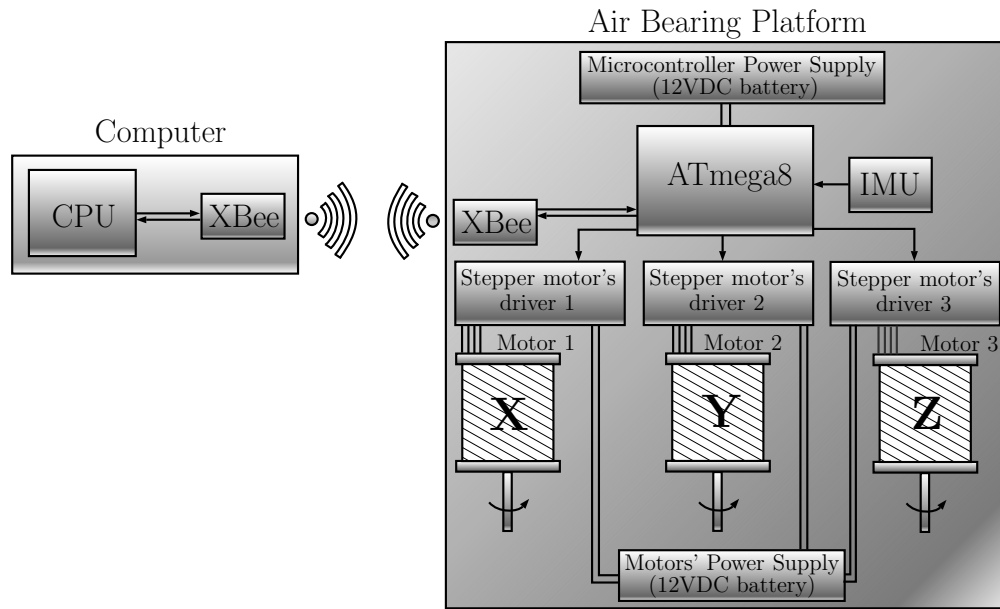
Fig. 4. Electronic components of the system.

2. Communication module: a XBee radio is used to make wireless communication with a computer that processes all the dynamic data collected.

3. Inertial Measurement Unit (IMU): an IMU with 9 Degrees of Freedom (DOF) is usedis used, specifically a magnetometer with 3 DOF, an accelerometer with 3 DOF and a gyroscope with 3 DOF.

4. Motor drivers: there are 3 driver boards used to control each of the 3 motors mounted on the table.

5. Stepper motors: there are 3 motors mounted on the table. They make possible the translational movement of masses in three non-redundant degrees of freedom.

6. Batteries: two lithium polymer batteries power the system.

A schematic of the electronic system components is shown in Fig. 4.

The Helmholtz cage

For control schemes based on magnetorquers, there must be a way to control the magnetic field of the test environment. To provide this capability, a Helmholtz cage was built.

The Helmholtz cage consists of a set of coils in which electric current runs in order to generate a magnetic field, as predicted by the Biot-Savart law of electromagnetics. By controlling the intensity and direction of this magnetic field, it is possible to simulate the orbital magnetic environment (Brewer 2012).

To this end, the design has six square coils, two for each axis of the cage, used to generate an homogeneous field according to the applied electric current. The magnitude of the generated field is given, in each of the axes of the cage, by the following equation

$$B = \frac{2\mu_0 N i}{\pi a} \cdot \frac{2}{(1 + \gamma^2)\sqrt{2 + \gamma^2}} \ . \tag{1}$$

where B is the generated field, μ_0 is the permeability of the environment, N is the number of wire turns in the coil, i is the applied current, a is half the side of the coil and γ, the relation between the distance within two coils in a pair and the side of a coil, is 0.5445. Further details on how Eq. (1) is achieved may be found in Batista et al. (2017), which also clarifies the definition of γ, an optimal construction parameter of the cage.

For the manufacturing of this equipment, it was decided to use "U" aluminum profiles, since the material used cannot possess magnetic characteristics, with dimensions of 1 inch base, 1 inch side and 3/32 inch thick ($1 \times 1 \times \frac{3}{32}$). The bars are attached using triangular aluminum side supports and M5 stainless steel screws in order to build 2.5 meters side squares. The structure is covered with enamelled copper wire, by means of constituting the coil.

Once the structure is assembled, the coils are connected to a direct electrical current supply (DC), responsible for feeding the system and generating the magnetic field. The current supply is automatically controlled through a software compatible with MATLAB that interprets the readings from magnetometers mounted in the air bearing table and calculate the current to be applied in order both to compensate the local magnetic field and establish the conditions suitable for the simulation of the orbital field needed. Fig. 5 shows the air bearing platform surrounded by the Helmholtz cage.

Measurements taken with the maximum supplying current of 6A allowed to conclude that the
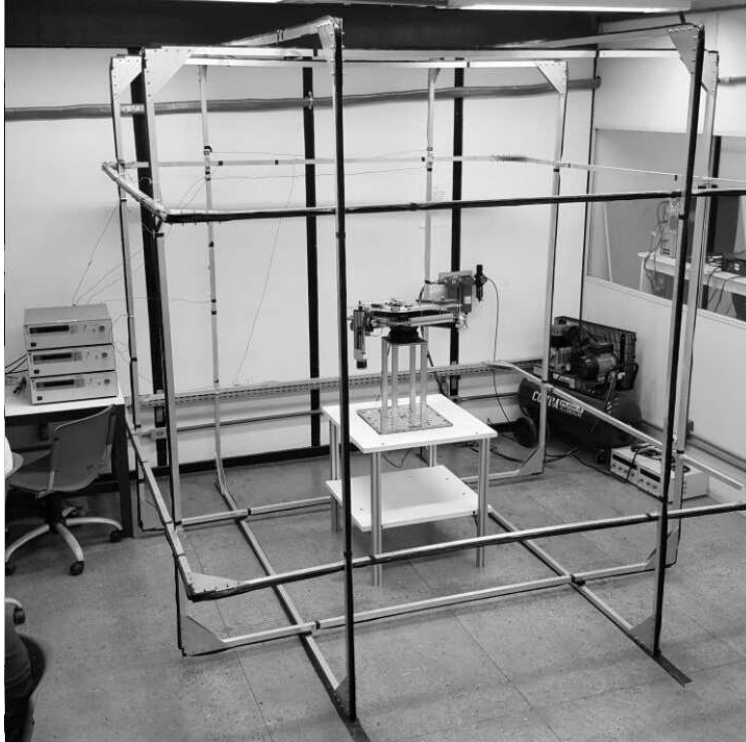
Fig. 5. The Helmholtz cage (image by authors).

cage is capable of generating approximately 180 μT in each of its axes, as can be seen in Fig. 6. It is possible to see the magnetic field in the laboratory environment with the Helmholtz cage turned off (initial portion of the graph) and turned on (final portion) in each axis. As can be seen in Fig. 6, the environmental magnetic field is -26 μT, 1.3 μT and 18.05 μT in the X, Y and Z axes of the cage, respectively. In other words, the cage is capable of nullifying the environmental magnetic field and still provide around 150 μT generation capability in each axis, which is sufficient for simulating most kinds of orbits. Another important aspect of the Helmholtz cage is the homogeneity of the magnetic field in its interior. The desired behaviour of the generated magnetic field in a specific instant is that it must remain constant, in direction and magnitude, in a volume which must cover the air bearing table entirely. In de Loiola et al. (2018), different tests were made in order to quantify the homogeneity of the field generated by the Helmholtz cage described in this work, reaching the conclusion that the magnetic field remains constant, given some variation tolerance, along 100 *cm* of each of the cage axes. Given that the air bearing table, when rotating, occupies a volume of

Silva, Approved on June 18th, 2018
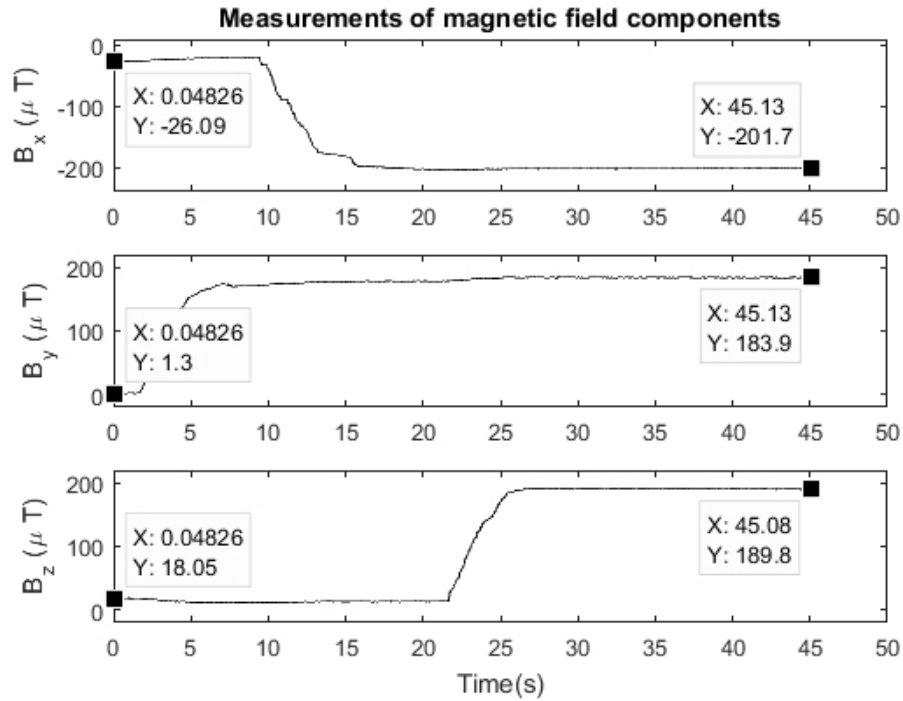
Fig. 6. Measurements of the environmental magnetic field taken at the center of the cage.

44 $cm \times 44\ cm \times 44\ cm$, the homogeneity requisite is guaranteed.

BALANCING TECHNIQUES

Reference systems

Two reference systems are established for the air bearing platform:

1. Inertial: the inertial frame, defined by the axes (X_i, Y_i, Z_i) is static and fixed in relation with the laboratory. Its origin is located at the CR of the air bearing.

2. Body: the body frame, defined by the axes (X_b, Y_b, Z_b) is fixed in relation with the air bearing table and moves with it. Its origin is coincident with the origin of the inertial frame.

Fig. 7 illustrates the relative position between the inertial and body frames when the table performs a roll movement.
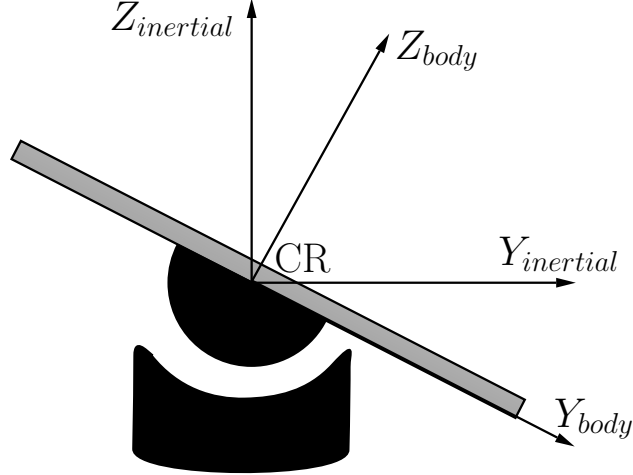
Fig. 7. Inertial and body frames during roll movement.

Platform dynamics

The platform can be modeled as a rigid body performing rotational movement and having its center of rotation fixed in both reference frames. For this system, the angular momentum taken at the center of rotation is given by Eq. (2) (Greenwood 1988),

$$\mathbf{H}_{CR} = \mathbf{r} \times M\mathbf{v}_{G} + \mathbf{H}_{G} , \tag{2}$$

where $\mathbf{H}_{G}$ is the angular momentum taken at the center of mass of the platform, M is the total mass of the system, $\mathbf{v}_{G}$ is the velocity vector at the center of mass and $\mathbf{r}$ is the CM offset, which is a vector starting from the CR and pointing to the CM.

The system dynamics is obtained from the Newton second law, resulting that the torque applied to the system is equal to the time derivative of its angular momentum, that is,

$$\boldsymbol{\tau}_{CR} = \frac{d\mathbf{H}_{CR}}{dt} , \tag{3}$$

in which the resulting external torque, $\boldsymbol{\tau}_{CR}$, may take into account various torque effects, such as aerodynamic drag torque, actuation torque and, mainly, the gravitational torque.

Evaluating the right hand side of Eq. (3), with $\mathbf{H}_{CR}$ given by Eq. (2), and taking into account the

Silva, Approved on June 18th, 2018

rate of change of vectors in rotating frames (Young 1998), it follows

$$\frac{d\mathbf{H}_{\text{CR}}}{dt} = (\mathbf{r} \times M\dot{\mathbf{r}}) + [\omega \times (\mathbf{r} \times M\dot{\mathbf{r}})] + \dot{\mathbf{H}}_{\text{G}} + (\omega \times \mathbf{H}_{\text{G}}) \tag{4}$$

in which ω is the angular velocity of body frame when rotating around the inertial frame. Eq. (4) can be written as

$$\mathbf{A} \cdot \dot{\omega} + \mathbf{B} = \boldsymbol{\tau}_{\text{CR}} , \tag{5}$$

in which the $\mathbf{A} = \mathbf{A}(M, \mathbf{r}, \mathbf{I})$ and $\mathbf{B} = \mathbf{B}(M, \mathbf{r}, \mathbf{I}, \omega)$ are 3×3 and 3×1 matrices and $\mathbf{I}$ is the inertia tensor of the system.

The acceleration vector can be obtained from Eq. (5) as

$$\dot{\omega} = (\mathbf{A})^{-1} \cdot (\boldsymbol{\tau}_{\text{CR}} - \mathbf{B}) , \tag{6}$$

which can be solved simultaneously with the Euler angular rates to simulate the platform behavior.

Dynamic model simplification

As could be seen in the subsection "Platform dynamics", the dynamics of the platform can be described by Eq. (6). Although this equation takes into account all the dynamic effects experimented by the platform, its implementation is not the most cost-effective since some simplifications can be done without affecting the performance of the balancing algorithm. For instance, assuming that ω and $\mathbf{r}$ in Eq. (6) have small magnitudes compared to the other terms, it follows that,

$$\begin{aligned} \dot{\omega} &= (\mathbf{A})^{-1}(\boldsymbol{\tau}_{\text{CR}} - \mathbf{B}) \\ &\approx (\mathbf{I})^{-1} \cdot \boldsymbol{\tau}_{\text{CR}} . \end{aligned} \tag{7}$$

Additionally, assuming that the aerodynamic torque is negligible and considering null actuation torque, the resultant torque is given solely by the gravitational torque, thus $\boldsymbol{\tau}_{\text{CR}} = \boldsymbol{\tau}_{\text{G}}$. This gravitational torque $\boldsymbol{\tau}_{\text{G}}$ can be determined by the cross product $\boldsymbol{\tau}_{\text{G}} = \mathbf{r} \times \mathbf{F} = \mathbf{r} \times M\mathbf{g}$, in which $\mathbf{F}$ is the moment force (weight) and $\mathbf{g}$ is the local gravity vector.

Since all the vectors in the model must be referred to the same reference system, the reference system fixed to the table (body-frame) is chosen. The superscripts i and b are used to identify the quantities referred to the inertial and body frames, respectively. Consequently, the local gravity vector is given in the inertial frame as $(\mathbf{g})^i = g \cdot \begin{bmatrix} 0 & 0 & -1 \end{bmatrix}^T$, in which g is a scalar with magnitude equal to the local gravity.

Using the Euler rotation matrix in the ZYX sequence that relates these two reference frames, $\mathbf{R}_i^b$, the local gravity can be described in the body frame as

$$(\mathbf{g})^b = \mathbf{R}_i^b \cdot (\mathbf{g})^i = \begin{bmatrix} g \cdot s_\theta \\ -g \cdot c_\theta s_\phi \\ -g \cdot c_\theta c_\phi \end{bmatrix}, \tag{8}$$

in which the ϕ, θ, ψ notation is used for the roll, pitch and yaw angles.

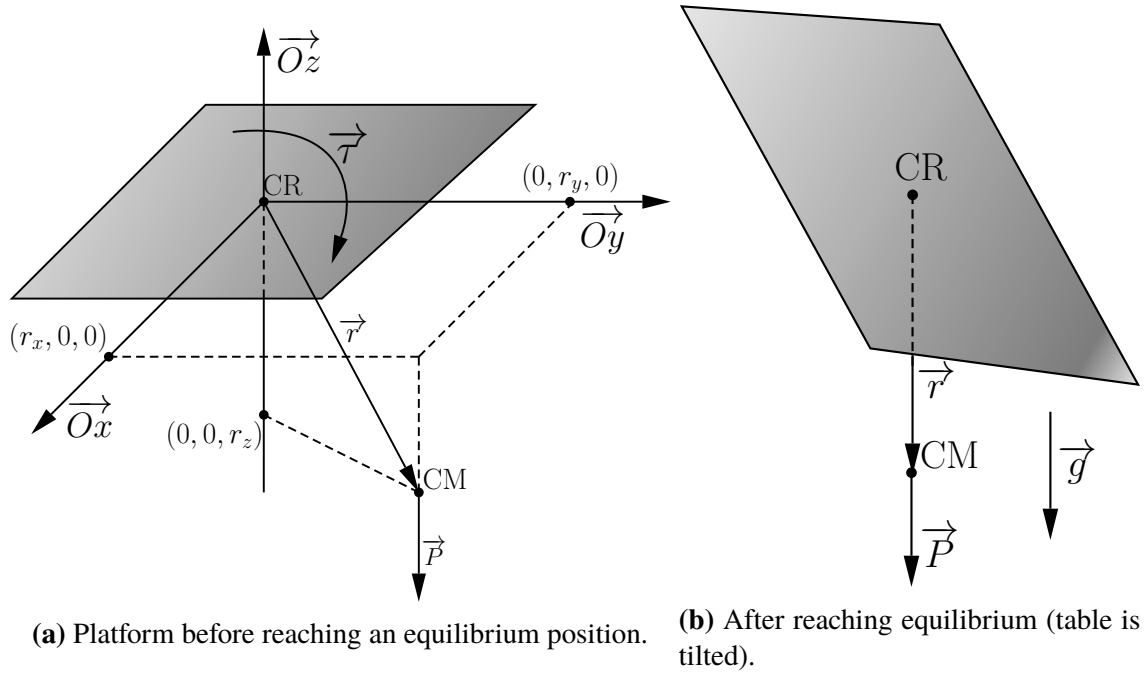Then, the gravitational torque may be calculated in the body frame as

$$\boldsymbol{\tau}_G = \mathbf{r} \times M\mathbf{g} = Mg \begin{bmatrix} r_z c_\theta s_\phi - r_y c_\theta c_\phi \\ r_z s_\theta + r_x c_\theta c_\phi \\ -r_y s_\theta - r_x c_\theta s_\phi \end{bmatrix}, \tag{9}$$

where the r_x, r_y and r_z scalars are the components of the unbalance vector $\mathbf{r}$.

Knowing that the inertia products have negligible magnitude compared with the principal moments,

$$\mathbf{I} \approx \begin{bmatrix} I_{xx} & 0 & 0 \\ 0 & I_{yy} & 0 \\ 0 & 0 & I_{zz} \end{bmatrix} \Rightarrow \mathbf{I}^{-1} = \begin{bmatrix} \frac{1}{I_{xx}} & 0 & 0 \\ 0 & \frac{1}{I_{yy}} & 0 \\ 0 & 0 & \frac{1}{I_{zz}} \end{bmatrix}. \tag{10}$$

Finally, replacing Eq. (10) and Eq. (9) in Eq. (7) the dynamic model of the platform can be

Silva, Approved on June 18th, 2018

(a) Platform before reaching an equilibrium position.

(b) After reaching equilibrium (table is tilted).

Fig. 8. Gravitational torque τ due to the presence of the gravitational force $\boldsymbol{P}$.

represented in a simplified manner as Eq. (11)

$$
\dot{\omega} =
\begin{bmatrix}
\frac{Mg}{I_{xx}}(-r_y c_\phi c_\theta + r_z s_\phi c_\theta) \\[2mm]
\frac{Mg}{I_{yy}}(r_x c_\phi c_\theta + r_z s_\theta) \\[2mm]
\frac{Mg}{I_{zz}}(-r_x s_\phi c_\theta - r_y s_\theta)
\end{bmatrix}. \tag{11}
$$

The batch estimation balancing algorithm

After mounting all the components described in the section "SYSTEM CONFIGURATION",

it is expected that the table would tend to reach an unbalanced position or, in other words, the

table would be tilted, as illustrated by Fig. 8. Being the center of mass (CM) in a position that is

displaced from the center of rotation (CR) of the table, a gravitational torque is produced around

the CR which tilts the platform.

The gravitational torque experienced by the table would interfere with the attitude control system

of any nanosatellite placed on the table, therefore, it is necessary to minimize it. This gravitational

torque is minimized by making the distance between the center of mass and the center of rotation

of the table as close as possible to zero.

A summary of the proposed algorithm is as follows:

1. First, dynamic data of the table are collected. This data are sent to the CPU through wireless communication. These data consists of the roll and pitch angles and the angular velocities of the table.

2. The CPU uses the data collected to make an estimation of the distance between the CM and the CR of the table.

3. The CPU evaluates the required actuation, i.e. how much each motor will have to move, and sends this command to the air bearing table through wireless communication.

4. After making the correction, dynamic data are collected again and the process is continued iteratively until the measured distance between the CR and the CM of the table reaches a predetermined threshold.

Considering the simplified version of the dynamic model of the testbed given in Eq. (11), the Least Squares Method (LSM) is used in order to improve the estimation of the components of the displacement vector (Young 1998). Firstly, Eq. (11) can be integrated over a short time period. In this way, the gyroscope data can be used and the only three unknowns that remains in this equation are the unbalance vector components. This is done under the assumption that the roll (ϕ) and pitch (θ) angles are almost constant during a small time step. The result of this is given by Eq. (12)

$$
\begin{aligned}
(\Delta\omega_x)_{t_2-t_1} &= \frac{-Mg\Delta t}{2I_{xx}} \left\{ \left[(c_\phi c_\theta)_{t_2} + (c_\phi c_\theta)_{t_1} \right] r_y - \left[(s_\phi c_\theta)_{t_2} + (s_\phi c_\theta)_{t_1} \right] r_z \right\}, \\
(\Delta\omega_y)_{t_2-t_1} &= \frac{Mg\Delta t}{2I_{yy}} \left\{ \left[(c_\phi c_\theta)_{t_2} + (c_\phi c_\theta)_{t_1} \right] r_x + \left[(s_\theta)_{t_2} + (s_\theta)_{t_1} \right] r_z \right\}, \\
(\Delta\omega_z)_{t_2-t_1} &= \frac{-Mg\Delta t}{2I_{zz}} \left\{ \left[(s_\phi c_\theta)_{t_2} + (s_\phi c_\theta)_{t_1} \right] r_x + \left[(s_\theta)_{t_2} + (s_\theta)_{t_1} \right] r_y \right\}.
\end{aligned}
\tag{12}
$$

that can be rewritten in the following manner

$$
\underbrace{\begin{bmatrix} \Delta\omega_x \\ \Delta\omega_y \\ \Delta\omega_z \end{bmatrix}}_{\Delta\Omega} = \underbrace{\begin{bmatrix} 0 & \phi_{12} & \phi_{13} \\ \phi_{21} & 0 & \phi_{23} \\ \phi_{31} & \phi_{32} & 0 \end{bmatrix}}_{\phi} \cdot \underbrace{\begin{bmatrix} r_x \\ r_y \\ r_z \end{bmatrix}}_{\mathbf{r}} , \tag{13}
$$

where the ϕ_{ij} terms are given as

$$
\begin{cases}
\phi_{12} = -\dfrac{Mg\Delta t}{2I_{xx}} \left((c_\phi c_\theta)_{t_2} + (c_\phi c_\theta)_{t_1} \right) , \\[2mm]
\phi_{13} = \dfrac{Mg\Delta t}{2I_{xx}} \left((s_\phi c_\theta)_{t_2} + (s_\phi c_\theta)_{t_1} \right) , \\[2mm]
\phi_{21} = \dfrac{Mg\Delta t}{2I_{yy}} \left((c_\phi c_\theta)_{t_2} + (c_\phi c_\theta)_{t_1} \right) , \\[2mm]
\phi_{23} = \dfrac{Mg\Delta t}{2I_{yy}} \left((s_\theta)_{t_2} + (s_\theta)_{t_1} \right) , \\[2mm]
\phi_{31} = -\dfrac{Mg\Delta t}{2I_{zz}} \left((s_\phi c_\theta)_{t_2} + (s_\phi c_\theta)_{t_1} \right) , \\[2mm]
\phi_{32} = -\dfrac{Mg\Delta t}{2I_{zz}} \left((s_\theta)_{t_2} + (s_\theta)_{t_1} \right) .
\end{cases} \tag{14}
$$

The LSM method is used because it finds a suitable estimation of the solution using all the data acquired from the sensors over time. It is also useful to prevent the occurrence of gross errors on the estimation caused by any kind of instantaneous sensor failure, since the estimation will not be

Silva, Approved on June 18th, 2018

evaluated using data of only one instant. Oversampling Eq. (13) results in the following system

$$
\underbrace{\begin{bmatrix} (\Delta\omega_x)_{t_0} \\ (\Delta\omega_y)_{t_0} \\ (\Delta\omega_z)_{t_0} \\ (\Delta\omega_x)_{t_1} \\ (\Delta\omega_y)_{t_1} \\ (\Delta\omega_z)_{t_1} \\ \vdots \end{bmatrix}}_{\Delta\boldsymbol{\Omega}_L} = \underbrace{\begin{bmatrix} 0 & (\phi_{12})_{t_0} & (\phi_{13})_{t_0} \\ (\phi_{21})_{t_0} & 0 & (\phi_{23})_{t_0} \\ (\phi_{31})_{t_0} & (\phi_{32})_{t_0} & 0 \\ 0 & (\phi_{12})_{t_1} & (\phi_{13})_{t_1} \\ (\phi_{21})_{t_1} & 0 & (\phi_{23})_{t_1} \\ (\phi_{31})_{t_1} & (\phi_{32})_{t_1} & 0 \\ \vdots & \vdots & \vdots \end{bmatrix}}_{\boldsymbol{\phi}_L} \cdot \underbrace{\begin{bmatrix} r_x \\ r_y \\ r_z \end{bmatrix}}_{\mathbf{r}} ,
\tag{15}
$$

that can be solved using the LSM providing the displacement vector shown in Eq. (16)

$$
\mathbf{r} = [\boldsymbol{\phi}_L^T \cdot \boldsymbol{\phi}_L]^{-1} \cdot \boldsymbol{\phi}_L^T \cdot \Delta\boldsymbol{\Omega}_L .
\tag{16}
$$

After having a proper estimation of the distance between the CR and the CM, the actuation system is responsible for compensating the unbalanced vector components. Assuming that all MMUs displace the same amount of mass in each of the three non-redundant translational degrees of freedom of the table, the actuation parameters are given by

$$
\Delta\mathbf{r}_{MMU} = -\frac{M}{m_{MMU}} \cdot \mathbf{r}_{CM} .
\tag{17}
$$

Variation of the inertia tensor

As one may notice, the inertia parameters of the platform are used in Eq. (16) in order to determine the unbalance vector components. These parameters are estimated in a CAD software and used to start the algorithm. For the current configuration of the platform, the inertia tensor is

Silva, Approved on June 18th, 2018

given by

$$\mathbf{I} = \begin{bmatrix} I_{xx} & I_{xy} & I_{xz} \\ I_{yx} & I_{yy} & I_{yz} \\ I_{zx} & I_{zy} & I_{zz} \end{bmatrix} = \begin{bmatrix} 0.265 & -0.014 & -0.035 \\ -0.014 & 0.246 & -0.018 \\ -0.035 & -0.018 & 0.427 \end{bmatrix} [kg \cdot m^2], \qquad (18)$$

and, as expected, the inertia products have much smaller magnitude than the principal moments of inertia. After each movement of a MMU, this initial inertia tensor is changed. These changes may be tracked in each iteration and incorporated to the algorithm to make corrections of the inertia tensor (Kim and Agrawal 2009).

SIMULATION AND TESTS

The tests conducted in this work have illustrated the quality of the balancing procedure based on batch estimation. By comparing the period of the platform oscillation with that of a simple pendulum, it was possible to notice the improvement of the results after each interaction of the balancing algorithm. Another way of verifying the balancing performance is to register the initial and final positions of the platform. Starting from a tilted position, the platform shall conclude the balancing procedure in an almost horizontal position, as the roll and pitch angles of the platform became approximately null. However, a fact should be clarified: the roll and pitch angles are expected to diminish to zero just in the case that the magnitude of the unbalance vector in the Z_b axis stays much higher than the magnitude of the horizontal plane component of the unbalance vector. Otherwise, the table could reach any other final inclination.

This fact points to a limitation concerning the balancing capability in the vertical axis (Z_b). Although the X_b and Y_b components became well balanced, there is still a considerable unbalance in the vertical axis of the platform since there is much more mass concentrated below its CR. There are several ways to avoid this problem, as for instance increase the mass that each MMU can move or simply add more weight above the CR of the platform. In this project, it was chosen to let the Z_b component of the unbalance vector to reach larger values by implementing an interface for mounting hardware above the initial configuration of the platform. The height of this plate related to the table is adjustable with screws.

TABLE 1. Evolution of the oscillation period along the iterations of the balancing algorithm.

Air bearing table with mounting plate			
		Oscillation period	
Iteration no.	$||r||$ (μm)	Calculated (s)	Measured (s)
Initial condition	4164.75	4.0827	4.3200
No. 1	3732.98	4.3124	4.7041
No. 2	3280.38	4.6003	4.7204
No. 3	2809.32	4.9710	5.4423
No. 4	2767.58	5.0084	5.5081
No. 5	2213.58	5.6002	5.8774
No. 6	2147.67	5.6855	6.2218
No. 7	1715.05	6.3622	6.9219
No. 8	1396.50	7.0506	7.7607
No. 9	1250.46	7.4510	8.5203
No. 10	910.12	8.7337	10.0773
No. 11	605.13	10.7108	12.9215
No. 12	289.42	15.4876	20.8118

This enabled the balancing process to position the CM even closer to the CR, as can be seen in Fig. 9. Also, the final period of oscillation of the table in the roll and pitch axes increased to 22.83 *s* and 20.81 *s*, respectively. In these new results, the MMUs were allowed to move a fixed maximum in each iteration, in order to better track the evolution of the unbalance vector. Table 1 presents the period of oscillation of the pitch axis starting from an arbitrary unbalance condition in which the MMUs were positioned randomly. The estimates of the unbalance vector components at the end of the balancing procedure were, for the X_b, Y_b and Z_b axes, -14.1 μm, -9.0 μm and -288.9 μm, respectively. The Z_b component did not achieve a magnitude similar to that obtained in the X_b and Y_b axes, since the balancing procedure stopped in order guarantee a stable position of the table, avoiding the inverted pendulum behaviour. This behaviour is characterized by the positioning of the CM above the CR, which makes the testbed move to the limit of the roll/pitch excursions.

Concerning the MMUs, each one has a total excursion of 134 *mm*. Each complete turn performed by the stepper motor on the crank of the MMU displaces a mass of approximately 0.7 *kg* for exactly 1 *mm* in the direction of the associate axis. Since the stepper motor driver is configured in the *200-step mode*, each turn corresponds to 200 voltage pulses sent to the driver. In other

Silva, Approved on June 18th, 2018
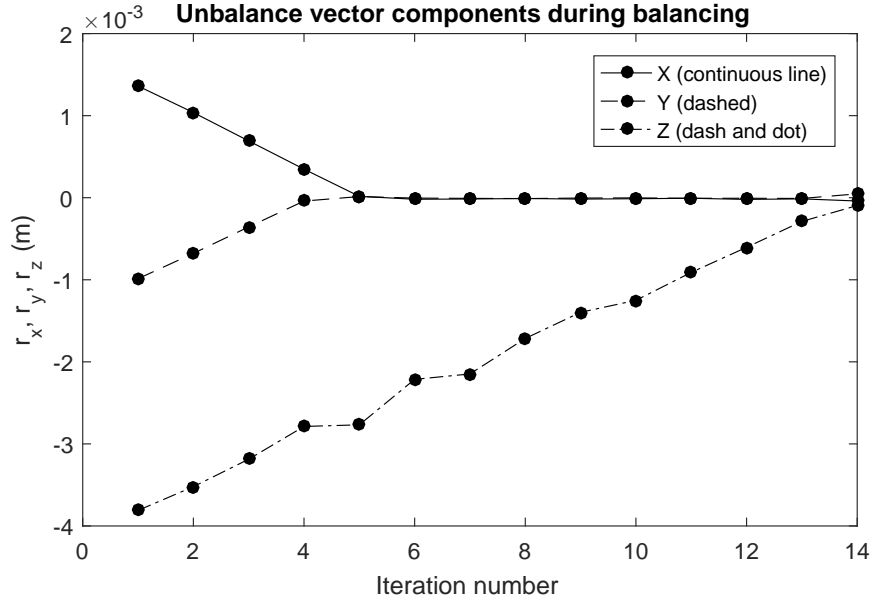
Fig. 9. Evolution of **r** components after increasing mass above the CR.

words, it is possible to perform just $\frac{1}{200}$ of a turn by sending a single pulse to the motor, meaning a displacement of 5 thousandths of a millimetre of the movable mass. Eq. (19) shows the unbalance vector variation $\Delta \mathbf{r}$

$$\Delta \mathbf{r} = \frac{m_{\text{MMU}}}{M} \begin{bmatrix} r_{mx} \\ r_{my} \\ r_{mz} \end{bmatrix}, \tag{19}$$

where r_{mi}, $i \in \{x, y, z\}$, are the displacements performed by each movable mass. Knowing that the testbed developed in this work weights 14 kg, Eq. (19) implies that the minimum change in any component of the unbalance vector **r** is 0.25 μm, whereas the maximum change is 6.7 mm. This range gives the maximum unbalance that can be compensated, as well as how close to the origin the MMUs can place the unbalance vector, what is in accordance with the initial and final values of $||\mathbf{r}||$ shown in Table 1. A 0.25 μm minimum step may indicate that a minimum of $3.5 \cdot 10^{-5}$ $N \cdot m$ gravitational torque is reachable (see Eq. (9)). However, there are some obstacles, such as the noise level of the sensors measurements, that makes impossible the gravitational torque to reach this minimum gravitational torque level, as is mentioned posteriorly.

Roll angle oscillation at the 3rd iteration

Single-Sided Amplitude Spectrum of ϕ**(t)**
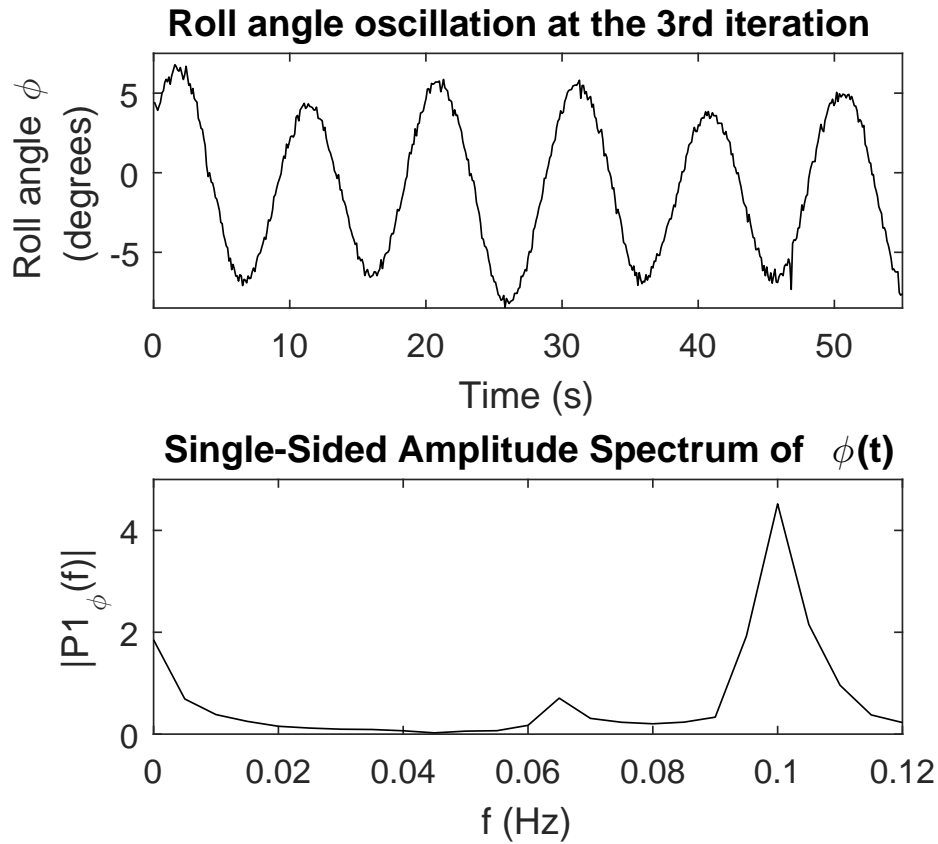
Fig. 10. Frequency spectrum using FFT.

Alternatively to the inspection method for estimating the oscillation period of the platform, in which the time difference between two peaks is measured, it is possible to analyze the frequency spectrum of these signals. In a second balancing test, the platform was first manually pre-balanced and 3 iterations of the balancing algorithm were executed. Applying the Fast Fourier Transform (FFT) to the oscillation signal obtained in the third iteration, it was possible to identify three main frequency components, as shown in Fig. 10. One is a constant component related to the steady-state equilibrium point of the platform and the other two components are related to the pendulum dynamics of the platform. The presence of two frequency components different from zero instead of one is related to the energy exchange between the roll and pitch axes. As can be seen in Fig. 10, the spectrum component of 0.1 Hz is dominant, what can also be noticed by checking the period of the signal in the time domain.

These results show that the proposed balancing method provided adequate balancing performance. As a mean of comparison, the values obtained for the x and y components present the same order of magnitude of similar works, as that shown in Liu et al. (2016), which reached a range of $5\mu m$ for the unbalance vector magnitude.

Additionally, an analysis of the convergence of the unbalance vector was also performed, similarly to that made by Young (1998). This analysis is important to define the minimum required length in order to provide good estimations of the unbalance vector. For that, the platform was excited with an initial angular momentum and sensor data were acquired during 5 minutes at a sampling frequency of $10\,Hz$. Then, the unbalance vector norm was calculated with various lengths of data, as well as the correspondent standard deviation. Fig. 11 shows the initial 50 seconds of this graph. The 5 initial samples of the estimated unbalance vector norm are not considered for the determination of the standard deviation graph, since they introduce considerable bias. The tests show that after 5 seconds there is already an expressive decay in the standard deviation of the norm estimation and, after 40 seconds, changes in the unbalance vector norm are minimal. In other words, 40 seconds of data acquisition at $10\,Hz$ is proved to be enough for a reasonably well estimation of the unbalance vector in the proposed tabletop testbed. One must also notice, in Fig. 11, the value to which the standard deviation converges, about $0.2\,\mu m$, which indicates the minimum trustworthy estimate of the unbalance vector and is related to the noise level in the IMU measurements.

Other balancing algorithms seen in the works published by Kim and Agrawal (2009) and Chesi et al. (2013) could also be implemented in the proposed platform. However, some facts must be mentioned: the results shown in Kim and Agrawal (2009) are based on an adaptive control method that cannot be tested in a platform equipped with balancing masses only. The work developed in Kim and Agrawal (2009) uses Control Moment Gyros (CMGs) which are responsible to track a particular angular momentum trajectory and the error is used as feedback to the adaptive control algorithm.

In this work, similarly to the work developed by Chesi et al. (2013), the only source of control
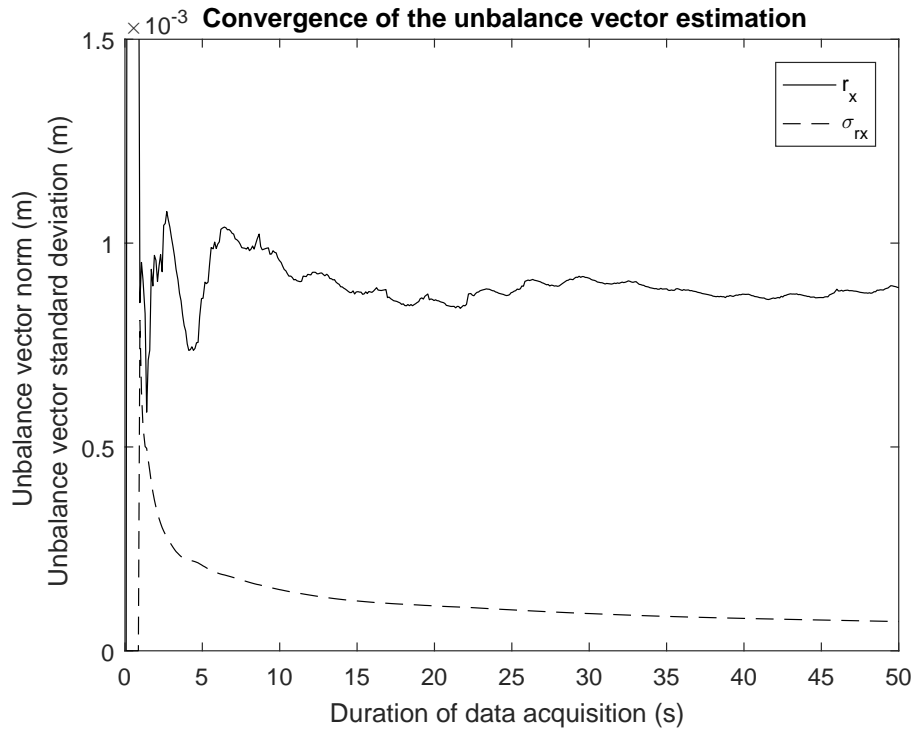
Fig. 11. Analysis of the LSM method convergence.

torque is that provided by the moving masses. Consequently, these torques are perpendicular to the

gravity field. To avoid this restriction of generating torque in the vertical axis, a two-stage balancing

algorithm was developed in which, in the first stage, only the unbalance vector components in the

transverse plane are compensated using adaptive feedback control law. Then, in a second stage,

an Unscented Kalman Filter is addressed in order to compensate for the last unbalance vector

component, which is parallel to the gravity field.

In this work, the main limitation of implementing the adaptive control scheme developed

by Kim and Agrawal (2009) is the absence of an alternative control torque source, whereas, for

the two-stage scheme developed by Chesi et al. (2013), the bottleneck is the processing capacity

of the adopted microcontroller. Both strategies utilize an onboard computer with high processing

capacity, differently from the Commercial off-the-shelf (COTS) microcontroller used in this work

which is already overwhelmed with the batch estimation implementation, even processing the LSM

data in an external computer.

The sensor performance must be also analyzed. In Kim and Agrawal (2009), it is mentioned that the tracking errors used as feedback tend to zero when there are no external torque disturbances. However, it is emphasized that the momentum tracking errors are noisy when the angular measurements are noisy. Thus, the mass balancing accuracy is highly sensitive to the quality of the sensor in this balancing method. In fact, a comparison between the batch estimation and the adaptive control made by Kim and Agrawal (2009) showed that, for some cases, the gravitational disturbances were better diminished with batch estimation and, when the adaptive control presented better results, the improvement was only about 46% at best. As shown in the section "SYSTEM CONFIGURATION", the gyroscopes measurement resolution provided by the IMU is of 0.01 rad/s or, equivalently, $0.5730^o/s$, much less than that provided by the IMU700 inertial measurement unit used in that work, which is of less than $0.025^o/s$ (more than 23 times better). Consequently, it is expected, *a priori*, that the implementation of Kim et al. method in this work would end in even worse results. In Chesi et al. (2015) it is also mentioned the influence of unmodeled noise effects in the measurements of the IMU. In this case, the IMU used - an ADIS16400 (Analog Devices) - provided $0.05^o/s$ of resolution. The advantages and disadvantages of each balancing method are summarized in Table 2.

In this context, the batch estimation method proved to be adequate in a low-cost system in which the sensor data may not have the desired precision. The LSM method, when applied with enough data, may suppress the noise influence.

Furthermore, as shown in Fig. 12, the platform oscillation decays with time, although it is assumed that there is no friction in the air bearing. This occurs because the aerodynamic drag torque, in fact, is present. As this effect is not predicted in the model simplification in Eq. (11), it may cause deviations in the unbalance vector estimation provided by the LSM method in case the data are collected for a long time. In other words, there is a trade off between the estimation convergence and its precision. The aerodynamic drag problem is also addressed in Chesi et al. (2013).

CONCLUSIONS

TABLE 2. Pros and Cons of each balancing method.

	Silva et al.
Pros	Satisfactory results are obtained using a low complexity algorithm. Does not require CMGs. Actuation is made using movable masses only. Less sensibility to sensor quality, since the noise effect is minimized by the Least Squares Method. Does not require an embedded controller, since calculations may be made in an external computer (consequently, there is no need of high processing capacity embedded in the onboard computer).
Cons	Does not solve the inverted pendulum problem. Correctness of the method is highly dependent on the accurate estimation of the inertia tensor. Method must be repeated several times until good balancing is achieved. Other methods may achieve better results.
	Chesi et al.
Pros	Does not require CMGs. Actuation is made using movable masses only. Capable of obtaining better results than those obtained with batch estimation.
Cons	Does not solve the inverted pendulum problem. Sensible to noise presence or low resolution in sensor measurements, in which case the batch estimation may obtain better results.
	Kim et al.
Pros	Solves the inverted pendulum problem. Capable of obtaining better results than those obtained with batch estimation.
Cons	Sensible to noise presence or low resolution in sensor measurements, in which case the batch estimation may obtain better results. Requires CMGs, *i.e.*, active torque actuators.

This article described a new platform developed at the University of Brasília for testing attitude determination and control systems of nanosatellites. The platform simulates the attitude dynamics of nanosatellites by using and air bearing table.

A LSM procedure has been proposed, based on the data from a COTS IMU, in order to reduce the distance between the center of mass and the center of rotation of the air bearing table. A
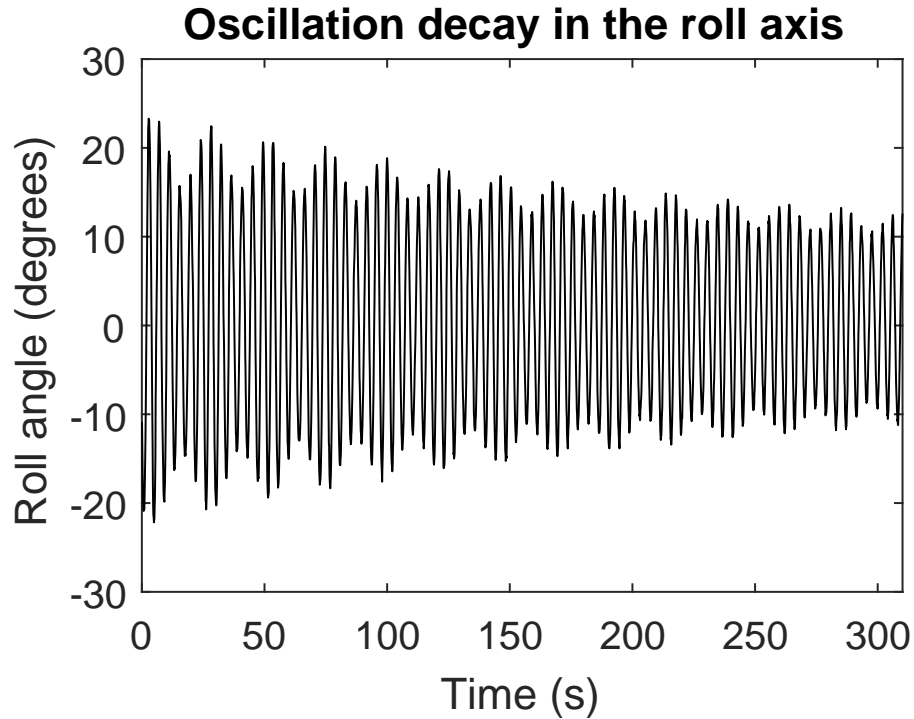
Fig. 12. Influence of the aerodynamic drag.

set of movable masses attached to the table are moved in accordance with the LSM algorithm and this allows the balancing of the platform. Results showed that, although only low-cost COTS electronic devices are used, the performance of the balancing system is satisfactory, since the achieved unbalance range is compatible with that shown in other works.

The testbed includes also an Helmholtz cage. The association between the testbed and the Helmholtz cage extends the range of simulation possibilities by making possible the simulation of the magnetic field of the Earth. Measurements taken during its operation showed that the cage is capable of generating enough magnetic field to run and test magnetic control algorithms, which will be done in future works.

Silva, Approved on June 18th, 2018

NOMENCLATURE

The following symbols are used in this paper:

$s_\bullet$ = Sine of the angle variable denoted by $\bullet$;

$c_\bullet$ = Cosine of the angle variable denoted by $\bullet$;

$\times$ = Standard cross product for vectors in $\mathbb{R}^3$;

ω = Vector of angular velocities [rad/s];

M = Total mass of the platform [kg];

m = Mass [kg];

ϕ = Roll angle [rad];

θ = Pitch angle [rad];

ψ = Yaw angle [rad];

I_{ij} = Components of the inertia tensor, $i, j \in \{x, y, z\}$;

$\mathbf{I}$ = Inertia tensor;

$\mathbf{r}$ = Unbalance vector or CM vector;

i = Applied current in the coil [A];

a = Length of half the side of the coil [m];

L = Length of the pendulum rod [m];

T = Oscillation period [s];

$\boldsymbol{\tau}$ = Torque [N.m];

γ = Aerodynamic coefficient of the platform;

$\mathbf{H}$ = Vector of angular momentum;

$\mathbf{v}$ = Vector of linear velocity;

$\mathbf{R}_i^j$ = Rotation matrix relating the i,j reference frames;

g = Magnitude of the local gravity vector;

t_i = Subscript that denotes the variable taken at time t_i;

G = Subscript related to the gravity field or vectors applied to the CM;

x,y,z = Subscripts used to denote scalar quantities related to the x, y or z axis;

b = Superscript of variables related to the body frame; and

i = Superscript of variables related to the inertial frame.

Silva, Approved on June 18th, 2018

REFERENCES

Batista, D. S., Granziera, F., Tosin, M. C., and de Melo, L. F. (2017). "Three-axial helmholtz coil design and validation for aerospace applications." *IEEE Transactions on Aerospace and Electronic Systems*.

Brewer, M. R. (2012). "Cubesat attitude determination and helmholtz cage design." M.S. thesis, Air Force Institute of Technology, United States.

Carletta, S. and Teofilatto, P. (2017). "Design and development of a full 5-dof testbed for testing nanosatellites formation flying, rendezvous and proximity operations." *9th International Workshop on Satellite Constellations and Formation Flying* (june).

Carrara, V. and Milani, P. G. (2007). "Controle de uma mesa de mancal a ar de um eixo equipada com giroscópio e roda de reação." *V SBEIN-Simpósio Brasileiro de Engenharia Inercial. Rio de Janeiro*, 26–29.

Chesi, S., Gong, Q., Pellegrini, V., Cristi, R., and Romano, M. (2013). "Automatic mass balancing of a spacecraft three-axis simulator: Analysis and experimentation." *Journal of Guidance, Control, and Dynamics*, 37(1), 197–206.

Chesi, S., Perez, O., and Romano, M. (2015). "A dynamic, hardware-in-the-loop, threeaxis simulator of spacecraft attitude maneuvering with nanosatellite dimensions." *Journal of Small Satellites*, 4(1), 315–328.

de Loiola, J. a. V. L., van der Ploeg, L. C., da Silva, R. C., Guimarães, F. C., Borges, R. A., and Borges, G. A. (2018). "3 axis simulator of the earth magnetic field." *Proceedings of the 39th IEEE Aerospace Conference*, IEEE, 1–8.

Gallardo, D. and Bevilacqua, R. (2011). "Six degrees of freedom experimental platform for testing autonomous satellites operations." *8th International ESA Conference on Guidance, Navigation and Control Systems*, 1–11.

Greenwood, D. T. (1988). *Principles of dynamics*. Prentice-Hall, Englewood Cliffs, New Jersey.

Kim, J.-J. and Agrawal, B. N. (2006). "System identification and automatic mass balancing of ground-based three-axis spacecraft simulator." *AIAA Guidance, Navigation, and Control Con-*

ference and Exhibit, 1–12.

Kim, J. J. and Agrawal, B. N. (2009). "Automatic mass balancing of air-bearing-based three-axis rotational spacecraft simulator." *Journal of Guidance, Control, and Dynamics*, 32(3), 1005–1017.

Liu, Y., Li, L., Fu, Z., Tan, J., and Li, K. (2016). "Automatic mass balancing of a spacecraft simulator based on non-orthogonal structure." *2016 UKACC 11th International Conference on Control (CONTROL)*, IEEE, 1–6.

Mittelsteadt, C. and Mehiel, E. (2007). "Cal poly spacecraft attitude dynamics simulator: Cp/sads." *AIAA Guidance, Navigation and Control Conference and Exhibit*, 1–24.

Peck, M. A., Miller, L., Cavender, A. R., Gonzalez, M., and Hintz, T. (2003). "An airbearing-based testbed for momentum control systems and spacecraft line of sight." *Advances in the Astronautical Sciences*, 114, 427–446.

Romano, M. and Agrawal, B. N. (2003). "Acquisition, tracking and pointing control of the bifocal relay mirror spacecraft." *Acta Astronautica*, 53(4), 509–519.

Saulnier, K., Perez, D., Tilton, G., Gallardo, D., Shake, C., Huang, R., and Bevilacqua, R. (2013). "Operational capabilities of a six degrees of freedom spacecraft simulator." *AIAA Guidance, Navigation, and Control (GNC) Conference*, 5253.

Schwartz, J. L., Peck, M. A., and Hall., C. D. (2003). "Historical review of air-bearing spacecraft simulators." *Journal of Guidance, Control and Dynamics*, 26, 513–522.

Silva, R. C., Rodrigues, U. A., Borges, R. A., Sampaio, M., Beghelli, P., Costa, S. G. P., Popov, B. T., Battistini, S., and Cappelletti, C. (2016). "A testbed for attitude and determination control of spacecrafts.." *Proceedings of the II IAA Latin American Cubesat Workshop*.

Thomas, D., Wolosik, A. T., and Black, J. (2018). "Cubesat attitude control simulator design." *2018 AIAA Modeling and Simulation Technologies Conference*, 1391.

Xu, Z., Chen, Y., Qi, N., Sun, Q., Fan, Y., and Wang, C. (2016). "Inertia parameters optimisation method for three-axis spacecraft simulator." *Electronics Letters*, 52(20), 1675–1677.

Young, J. S. (1998). "Development of an automatic balancing system for a small satellite attitude

492   control simulator." M.S. thesis, Utah State University, United States.